Neurobiology of Disease

Focal Increases of Axoplasmic Ca^{2+}, Aggregation of Sodium–Calcium Exchanger, N-type Ca^{2+} Channel, and Actin Define the Sites of Spheroids in Axons Undergoing Oxidative Stress

Anna G. Barsukova,[1] Michael Forte,[2] and Dennis Bourdette[1,3]

[1]Department of Neurology and [2]Vollum Institute, Oregon Health & Science University, Portland, Oregon 97239, and [3]VA MS Center of Excellence–West and Neurology Service, Department of Veterans Affairs, Portland, Oregon 97239

Axonal spheroids occur as part of the pathology of a variety of neurologic diseases. Reactive oxygen species (ROS) trigger formation of spheroids, axonal severing, and Ca^{2+} overload. The mechanisms by which ROS lead to the spheroid formation at specific axonal sites remain elusive. Here, using adult mouse primary neurons, we investigate the role of Ca^{2+}, its regulating systems, and cytoskeletal changes in formation of axonal spheroids triggered by ROS. The results reveal that dramatically higher axoplasmic Ca^{2+} levels occur at the sites of axonal spheroids than in the rest of the axon. High focal axoplasmic Ca^{2+} levels correlate with focal aggregation of the reverse Na^+/Ca^{2+} exchanger 1, voltage-gated N-type Ca^{2+} channel α1B subunit, and actin at the sites of spheroids in individual axons. This study provides new insights into the mechanism of a spheroid formation at specific sites along axons undergoing oxidative stress and a basis for new neuroprotective strategies.

Introduction

Oxidative stress is common in a number of neurologic diseases, such as multiple sclerosis (MS), ischemia, amyotrophic lateral sclerosis, Alzheimer's disease, Huntington's disease, and Parkinson's disease (Sayre et al., 2008). Characteristic morphology of neurodegeneration, axonal spheroids, is also found in these disorders. In a mouse model of MS, experimental autoimmune encephalomyelitis (EAE), it has recently been shown that inflammatory processes lead to an increase in extracellular reactive oxygen species (ROS) in acute EAE lesions (Nikić et al., 2011). This *in vivo* study established a direct link between high extracellular ROS and the formation of axonal spheroids and subsequent severing of the axons at the site of spheroid formation. These morphological changes are characteristic of Wallerian-like degeneration (Beirowski et al., 2010), which is recognized as a primary pathologic event in a number of neurologic disorders where it precedes neuronal cell body injury. These observations suggest that ROS may be an important cause of formation of axonal spheroids and degeneration in a variety of neurologic diseases.

Formation of axonal spheroids begins with the creation of smaller axonal swellings (Coleman, 2005). To date, a number of events associated with spheroid formation have been described and include increases in extracellular ROS, global axoplasmic Ca^{2+} increases, aggregation of dysfunctional mitochondria, and protease activation (Coleman, 2005; Nikić et al., 2011; Wang et al., 2012). Essential for neuroprotective strategies, spheroid formation may be a reversible process as shown by a direct application of an antioxidant mixture *in vivo* (Nikić et al., 2011). However, the molecular details of how spheroids form at particular axonal sites are uncertain.

Extracellular ROS trigger an increase in neuronal Ca^{2+} (Barsukova et al., 2011b), which has been steadily emerging as a key player in neurodegeneration. Quenching or removal of extracellular Ca^{2+} has been shown to be most effective in preventing spheroid formation in neuronal cultures (Beirowski et al., 2010). Regulation of axoplasmic Ca^{2+} involves interplay of Ca^{2+} channels, Na^+/Ca^{2+} exchanger on the axolemma, and endoplasmic reticulum and mitochondria within the axoplasma. Therefore, elucidating the role of these Ca^{2+}-regulating systems in spheroid formation is critical to a development of neuroprotective strategies. Here, using high-resolution imaging, we investigate Ca^{2+}-regulating systems and focal Ca^{2+} elevation at sites of axonal spheroids in live cortical neurons from adult and postnatal mice during exposure to ROS. Our results establish specific roles for the reverse Na^+/Ca^{2+} exchanger 1 (NCX1) and voltage-gated N-type Ca^{2+} channel (VGCC) α1B subunit in ROS-mediated focal axoplasmic Ca^{2+} elevation at the sites of axonal spheroid

Received Jan. 26, 2012; revised June 26, 2012; accepted July 4, 2012.

Author contributions: A.G.B. designed research; A.G.B. performed research; A.G.B., M.F., and D.B. analyzed data; A.G.B., M.F., and D.B. wrote the paper.

This work was supported by grants from the National Institutes of Health (1R01NS057433 and 1R01GM069883; training grant T32 NS007381), the National Multiple Sclerosis Society (CA-1055-A-3), the Department of Veterans Affairs, the Office of Research and Development, the Biomedical Laboratory of Research and Development, the Laura Fund for Innovation in Multiple Sclerosis Research, the Nancy Davis Center Without Walls, and the St. Laurent Foundation of Vancouver. The study was also supported by NIH NINDS Grant P30NS061800.

Correspondence should be addressed to Anna G. Barsukova, Oregon Health & Science University, 3181 SW Sam Jackson Park Road, Portland, OR 97239. E-mail: barsukov@ohsu.edu.

DOI:10.1523/JNEUROSCI.0408-12.2012

 0270-6474/12/3212028-10$15.00/0

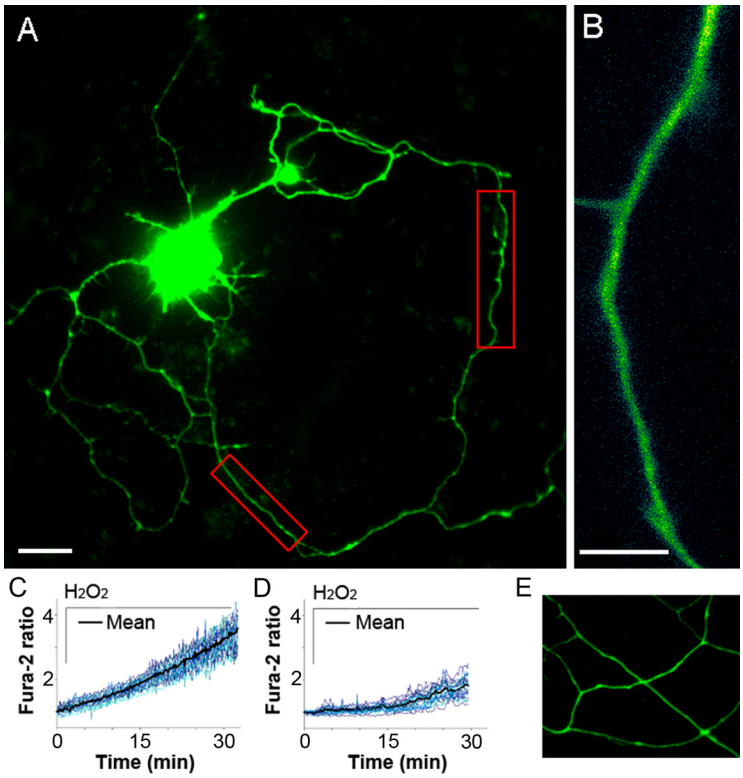

Figure 1. Real-time axoplasmic Ca^{2+} response to ROS in adult and postnatal cortical neurons. ***A***, Image of a cultured cortical neuron from an adult mouse loaded with fura-2 (60×, oil). In red boxes are 20–30 μm axonal segments chosen for high-resolution imaging. Scale bar, 10 μm. ***B***, Representative axonal segment used for axoplasmic Ca^{2+} analysis (super-high resolution, 150×, oil). Scale bar, 5 μm. ***C***, Axoplasmic Ca^{2+} response to 100 μM H_2O_2 in adult neurons ($n = 16$ cells). ***D***, Axoplasmic Ca^{2+} response in P0 neurons ($n = 23$ cells). Before treatments, axoplasmic Ca^{2+} levels among neurons of both ages were similar (0–1 min). ***E***, Absence of axonal spheroids in P0 neurons at 30 min of H_2O_2 exposure ($n = 18$ cells).

formation. The findings suggest that NCX1 and VGCC aggregation, associated with actin aggregation, drives dramatic focal increases of axoplasmic Ca^{2+}. Prevention of ROS-driven focal Ca^{2+} rise, spheroid formation and axonal severing in the presence of ROS is successfully achieved by inhibition of the reverse NCX1, N-type, and L-type VGCCs or with the actin stabilizing agent. This study provides new insights into the mechanism of a spheroid formation at specific sites along axons undergoing oxidative stress.

Materials and Methods

Cell cultures and transfection. Primary cortical cultures were prepared from adult 2- to 4-month-old and postnatal day 0 (P0) wild-type B6 mice of either sex as described previously (Nathan et al., 2004; Barsukova et al., 2011a,b). The entire cerebral cortex was dissected from the brain and placed in 2 ml of B27/Hibernate A medium (B27/HA; Invitrogen) with 0.5 mM glutamine (Sigma-Aldrich) at 4°C. The cortex was sliced (0.5 mm thickness) and transferred to a 50 ml tube containing 5 ml of B27/HA. After warming for 8 min at 30°C, slices were digested with 6 ml of a 2 mg/ml papain (Sigma-Aldrich) solution in B27/HA for 30 min at 30°C in a gyrating water bath. The slices were transferred to 2 ml of B27/HA. After 2 min at room temperature, the slices were triturated 10 times with a siliconized 9 inch Pasteur pipette and allowed to settle for 1 min. Approximately 2 ml of the supernatant was transferred to another tube, and the sediment was resuspended in 2 ml of B27/HA. The above step was repeated twice, and a total of 6 ml was collected. The resultant supernatant was subjected to density gradient centrifugation at 800 × *g* for 15 min. The density gradient was prepared in four 1 ml layers of 35, 25, 20, and 15% Optiprep (Invitrogen) in B27/HA medium (v/v). Debris above the neuron-enriched fraction was discarded. The neuron-enriched fraction was collected and diluted in 5 ml of B27/HA. After centrifuging twice at 200 × *g* for 2 min., the cell pellets were resuspended in 3 ml of B27/Neurobasal A medium (Invitrogen) with 0.5 mM glutamine and 0.01 mg/ml gentamicin (Sigma-Aldrich). For transfection, neuronal pellets were resuspended in 100 μl of nucleofection solution with 3 μg/ml of each plasmid construct and electroporated following an electroporation system (Amaxa Biosystems) for neurons, modified by the use of a Ca^{2+}-free buffer immediately after the electroporation, which maintained neuronal viability (Barsukova et al., 2011a,b). A total of 3×10^4 cells were plated in 30 μl aliquots in the center of glass coverslips (25 mm diameter) that were coated overnight with poly-D-lysine (50 mg/ml; Sigma-Aldrich). After a 1 h incubation in a humidified incubator at 37°C and 5% CO_2, each coverslip was rinsed with B27/HA and transferred to a six-well plate containing B27/neurobasal A medium. Routinely, 10% of adult neurons were successfully transfected, and the signal was detectable at 48 h after transfection.

Constructs. For imaging of axonal β-tubulin III, F-actin, and mitochondria, neurons were transfected with genetically encoded constructs EGFP-TubbIII, RFP-actin, and mito-RFP, respectively, kindly provided by Dr. G. Banker (Oregon Health & Science University, Portland, OR).

Reverse Na^+/Ca^{2+} exchanger and Ca^{2+} channel blockers. Reverse Na^+/Ca^{2+} exchanger was blocked with 1 μM KB-R7943 (Sigma-Aldrich), the concentration below the range capable of blocking mitochondrial Ca^{2+} uniporter. N-type VGCCs were blocked by a 30 min pretreatment with 50 nM ω-conotoxin GVIA (Sigma-Aldrich). L-type VGCCs were blocked by pretreatment with 1 μM amlodipine (Sigma-Aldrich) for 30 min.

Ca^{2+} and Na^+ measurement. For axoplasmic Ca^{2+} measurements, neurons were loaded with ratiometric Ca^{2+} dyes fura-2 AM or fura-FF (340 and 380 nm excitation, 505 nm emission; Invitrogen) (Fig. 1*A*). The results reported by fura-2 (high-affinity calcium indicator) were compared with cytosolic Ca^{2+} response reported by fura-2FF (low-affinity calcium indicator). Consequently, fura-FF was not used because it did not accurately report changes in Ca^{2+} levels in neurons of either age in response to H_2O_2. For axoplasmic Na^+ measurements, neurons were loaded with ratiometric Na^+ dye SBFI (340 and 380 nm excitation, 505 nm emission; Invitrogen). Cells were incubated with 5 μM fura-2 AM or SBFI in imaging buffer (in mM: 142 NaCl, 4 $NaHCO_3$, 10 Na-HEPES, 2.5 KCl, 1.2 $MgCl_2$, 2 $CaCl_2$, and 10 glucose, pH 7.4) containing 2% BSA (Sigma-Aldrich) and 0.01% pluronic acid at 37°C for 20 min or 2 h, respectively (Barsukova et al., 2011a,b). Cells were washed with imaging buffer containing 0.25% BSA for 10 min at 37°C before recording.

Fluorescence live imaging. Imaging was performed after 4–5 d in culture. Neurons were treated with 50 or 100 μM H_2O_2 for 30 min starting at 1 min in the presence of a 5% CO_2 air mixture at 37°C (heated stage; Warner Instruments). Before H_2O_2 treatment, axoplasmic Ca^{2+} or Na^+ levels among neurons of either age were similar. Neurons were also treated with 90 mM potassium chloride (Sigma-Aldrich). Imaging was performed using an inverted microscope (IX81; Olympus) equipped with a cooled CCD camera (Cascade II; Intelligent Imaging Innovations), a high-speed wavelength switcher (Lambda DG-5; Sutter Instruments) controlled by SlideBook software (Intelligent Imaging Innovations), and appropriate Chroma filters. Exposure time was 500 ms, and frames were taken every 10 s. Axoplasmic Ca^{2+} and Na^+ were evaluated in various

axonal segments, from 2 to 30 μm, with 1500 magnification (Olympus; 150×, UPlan, NA 1.45, oil) (Fig. 1*A*,*B*).

Immunocytochemistry. Neurons were fixed with ice-cold acetone for 5 min, rinsed with cold PBS, permeabilized for 15 min in 0.02% Triton X-100, and blocked in 1% BSA for 1 h. Neurons were then treated with rabbit anti-calcium channel (α1B subunit, N-type channel) antibody (Sigma-Aldrich) or NCX1 antibody (Covance), 1:1000 in 1% BSA for 2 h. After three washes with PBS, neurons were treated with appropriate anti-rabbit RFP or anti-mouse GFP secondary antibodies (1:200; Invitrogen) for 30 min. After three washes with PBS, neurons were coated with anti-photobleach oil, and coverslips were sealed.

Image analysis. Fluorescence changes in axoplasm were evaluated using SlideBook software version 4.2.0. The background fluorescence was taken from fields not containing axons. Data obtained from 10–50 segments per axon were averaged to represent the response per cell (10–15 cells per experiment).

Statistical analysis. Each experiment was replicated three times using neurons obtained from three different animals per age ($n = 3$). Data from each experiment were analyzed by *t* test or one-way ANOVA with SPSS statistical software. The data from all evaluated cells from all animals per age group are presented as mean ± SEM in the bar graphs described in Results.

Results

Neuronal model

To investigate the effect of extracellular ROS on axoplasmic Ca^{2+} and the role of elevated Ca^{2+} in spheroid formation, we established a neuronal model based on primary cultured cortical neurons from adult mice after comparing these cultures with the more commonly used P0 primary cortical neurons. We used pathophysiological levels of hydrogen peroxide previously detected in the brain *in vivo* during ischemia (Hyslop et al., 1995) and used in an *in vivo* spheroid formation study (Nikić et al., 2011). In each case, axoplasmic Ca^{2+} was assessed with fura-2 during 30 min exposure to H_2O_2 at 100 μM. A remarkable difference in axoplasmic Ca^{2+} elevation, measured in 20–30 μm axonal segments, was detected between neuronal ages. By 15 min, Ca^{2+} in P0 axons did not significantly change from the base level, while in adult axons it doubled (Fig. 1*C*,*D*). By 30 min, P0 axons had only a 1.8-fold fura-2 fluorescence rise, whereas in adult axons the fluorescence rise reached a 3.6-fold increase, twice the level of P0 axons (Fig. 1*C*,*D*; Student's *t* test, $^{**}p < 0.01$). By 30 min, adult axons showed formation of spheroids (Fig. 2*A*,*B*) whereas the P0 axons did not (Fig. 1*E*). There were thus significant differences in responses of cultured adult and P0 axons within the first 30 min of exposure to H_2O_2. For all other studies, we selected the adult neurons based on rapid dynamic changes in their axons, which were not observed in postnatal cultures and as more representative of what occurs in neurons in adult EAE mice (Nikić et al., 2011) and in adult-onset diseases in humans, such as MS.

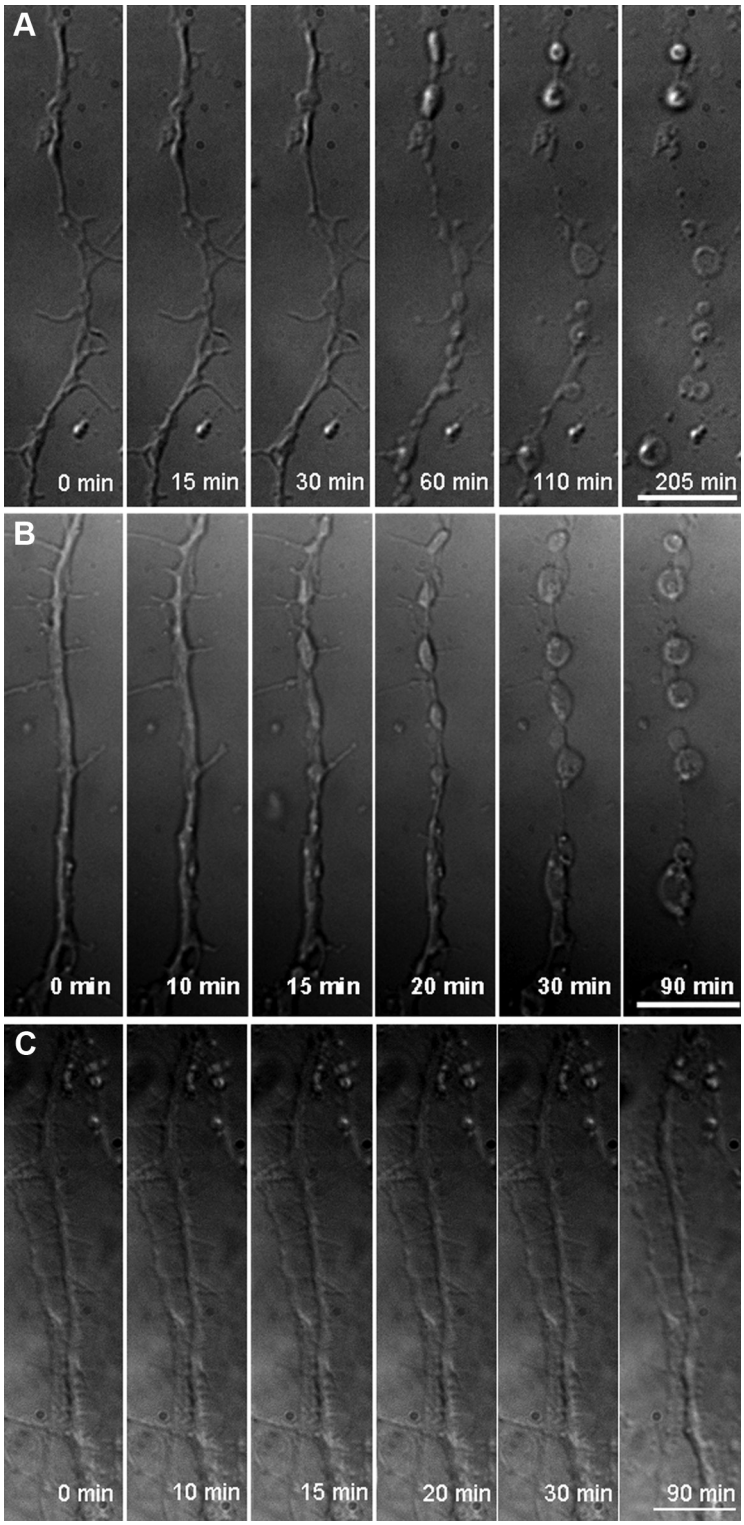

Figure 2. Spheroid formation and severing of axons triggered by ROS in live adult neurons. ***A***, Swellings form at 30 min, spheroids form at 60 min, and an axon severs by 205 min in the presence of 50 μM H_2O_2 ($n = 9$ cells). ***B***, Swellings appear at 15 min, spheroids appear by 30 min, and an axon severs by 90 min in the presence of 100 μM H_2O_2 ($n = 15$ cells). ***C***, In the absence of H_2O_2, imaging stress leads only to axonal swellings by 90 min ($n = 5$ cells) (150×, oil). Scale bar, 10 μm.

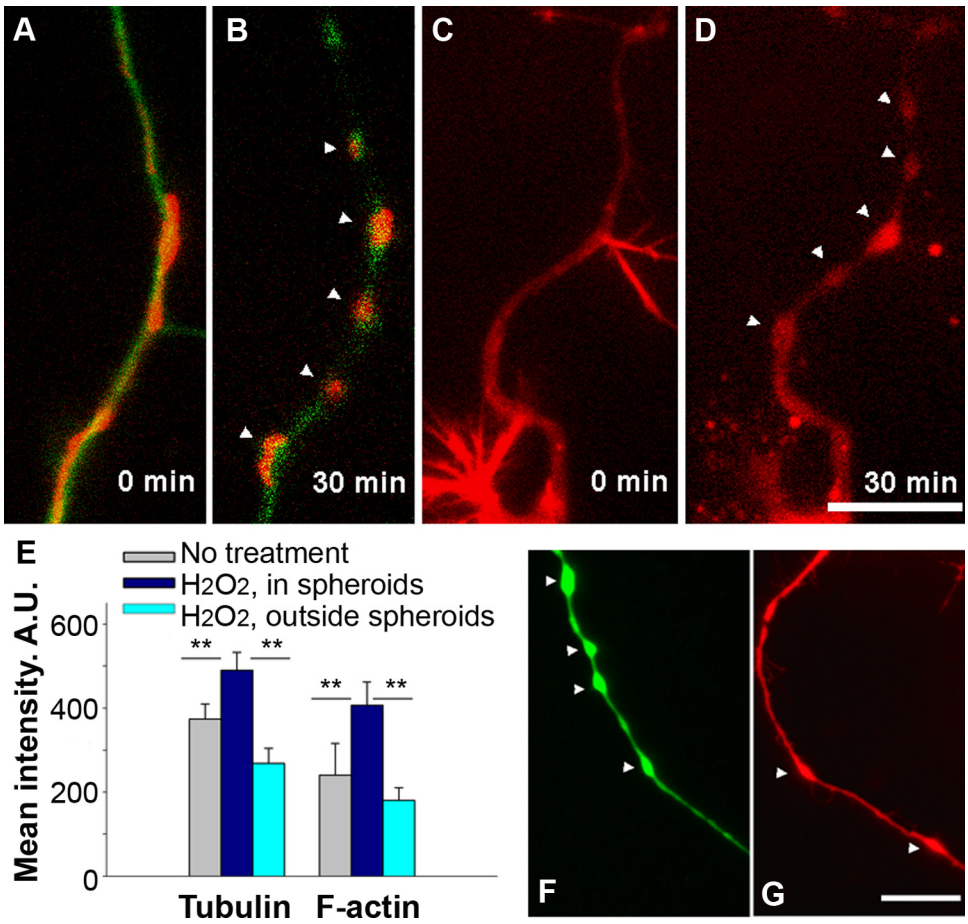

Figure 3. Cytoskeletal changes in axons of live adult neurons during spheroid formation triggered by ROS. ***A***, Axon of a neuron transfected with fluorescent constructs labeling β-tubulin III (green) and mitochondria (red). ***B***, Colocalization of rounded mitochondria and tubulin in spheroids after 30 min exposure to 100 μM H_2O_2 ($n = 12$ cells). ***C***, Neurons transfected with a fluorescent construct for F-actin (red). ***D***, Aggregation of F-actin in spheroids after 30 min exposure to 100 μM H_2O_2 ($n = 15$ cells). ***E***, Quantification of fluorescence intensities of tubulin and F-actin inside and outside the spheroids at 30 min (one-way ANOVA, $^{**}p < 0.001$). A.U., Arbitrary units. ***F***, Pretreatment with 1 μM Taxol does not prevent spheroid formation (image at 30 min of H_2O_2 exposure; $n =$ 10 cells). ***G***, Pretreatment with cytochalasin D (10 μg/ml) attenuates spheroid formation (image at 30 min of H_2O_2 exposure; $n = 9$ cells; 150×, oil). Scale bars, 10 μm.

Spheroid formation and axoskeletal changes

Axonal morphology and axoskeletal changes in live adult neurons were examined during oxidative stress with high magnification (150× lens). Morphology of 40–50 μm axonal segments was followed with time-lapse differential interference contrast (DIC) microscopy. H_2O_2 was continuously present starting at min 1. After continuous exposure to H_2O_2, axons underwent progressive morphologic changes. Formation of focal swellings in axons began at ~30 min in response to 50 μM H_2O_2 (Fig. 2*A*) and ~15 min in response to 100 μM H_2O_2 (Fig. 2*B*). Swellings progressed to spheroids around 60 and 30 min for 50 μM H_2O_2 and 100 μM H_2O_2, respectively (Fig. 2*A*,*B*). At the same time, segments of axons between the spheroids decreased in diameter. Disruption of axons at spheroids occurred at ~205 min with 50 μM H_2O_2 and ~90 min with 100 μM H_2O_2 (Fig. 2*A*,*B*). Therefore, the timing of development of swellings, formation of spheroids, and axonal severing occurred in an H_2O_2 concentration-dependent manner. To minimize the contribution of the imaging stress, which led to axonal swellings by 90 min (Fig. 2*C*) and severing at about 6 h in the absence of H_2O_2, 100 μM H_2O_2 was chosen for all other experiments.

The formation of spheroids coincided with changes in mitochondria, β-tubulin III, and F-actin. Changes in mitochondrial morphology in live neurons and its colocalization with spheroids were detected by the use of mitochondrially targeted genetic construct mito-RFP (Fig. 3*A*,*B*). Swelling and rounding of mitochondria began ~15 min of exposure. Swollen mitochondria were localized within the spheroids by 30 min.

β-Tubulin III and F-actin were labeled with the genetic constructs EGFP-TubbIII and RFP-actin, respectively. Before the application of H_2O_2, actin was more concentrated in the philopodia of axon terminals and at points of axonal branching, whereas tubulin was evenly distributed along axons. Dynamic changes in tubulin and F-actin were detected during spheroid formation. Significantly higher fluorescence density of tubulin and actin labeling was detected in spheroids than in segments outside the spheroids of live neurons at 30 min with 100 μM H_2O_2 exposure (Fig. 3*A*–*E*). Faster actin responses in a form of aggregation occurred in the retracting philopodia and small axonal branches than along the axon during the H_2O_2 treatment (Fig. 3*C*,*D*).

Pretreatment of neurons with tubulin-stabilizing agent Taxol did not prevent spheroid formation (Fig. 3, compare *F*, *B*). Pretreatment with the actin-stabilizing agent cytochalasin D greatly attenuated spheroid formation (Fig. 3, compare *G*, *D*); only formation of swelling was observed at 30 min, which did not progress to spheroid formation. These data demonstrate that spheroid formation and narrowing of an axon between spheroids is accompanied by active cytoskeletal restructuring during oxidative stress and, as has been described *in vivo*, by morphologic changes in mitochondria (Nikić et al., 2011).

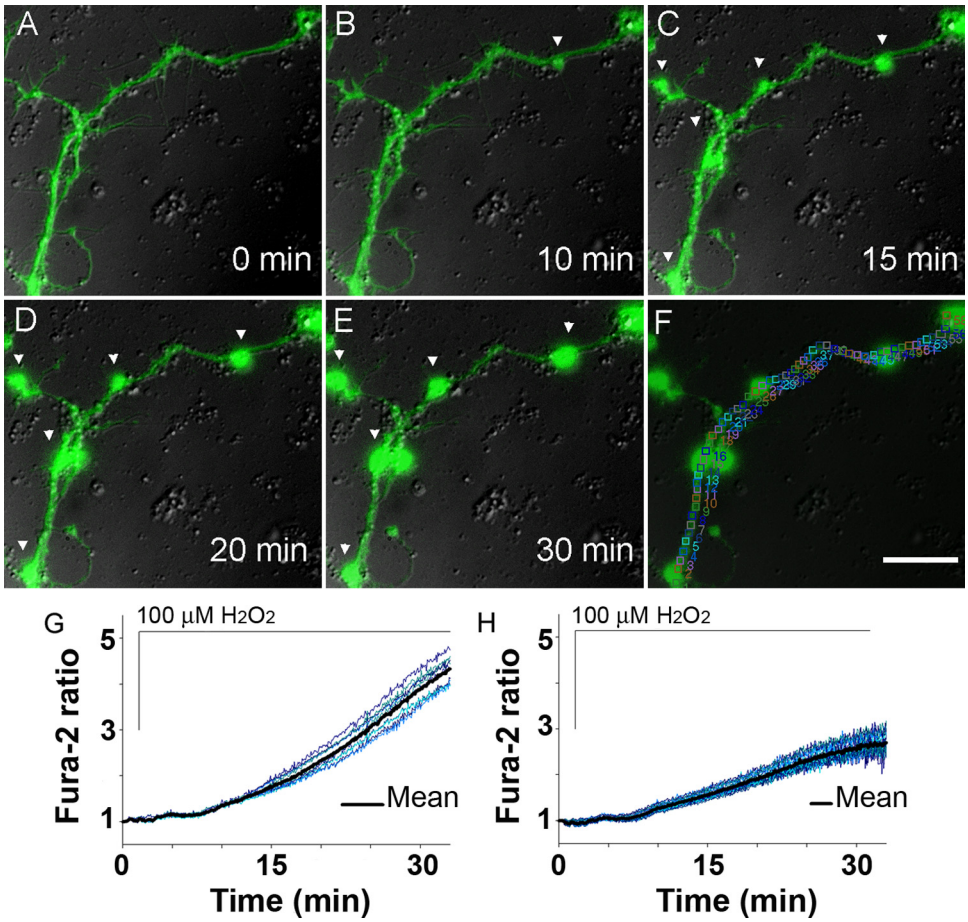

Figure 4. Ca^{2+} in an axon of a live adult neuron during spheroid formation triggered by ROS. ***A–E***, Axonal swelling formation at 15 min, followed by spheroids at 20–30 min, coincides with focal Ca^{2+} increase at spheroid sites as assessed by fura-2 (green) and DIC (gray) during 30 min exposure to 100 μM H_2O_2 ($n = 15$ cells; 150×, oil). Scale bar, 10 μm. ***F***, Representative 2–3 μm regions chosen for focal Ca^{2+} analysis. ***G***, Ca^{2+} levels at the sites of spheroids. ***H***, Ca^{2+} levels in axonal segments between the spheroids.

Axoplasmic Ca^{2+} in spheroids

Global increases of axoplasmic Ca^{2+} have been previously associated with axonal spheroid formation and disruption. Because distinct microdomains with transient high focal Ca^{2+} were previously demonstrated in healthy neurons (Chen et al., 2011), we sought to determine whether axoplasmic Ca^{2+} increased uniformly along axons undergoing oxidative stress or whether there might be focal increases at sites of spheroid formation. To determine this, we measured axoplasmic Ca^{2+} response to H_2O_2 in 2–3 μm axonal segments (Fig. 4*F*) instead of 20–30 μm segments used in initial studies (Fig. 1*A*). Such measurements allowed for comparison of Ca^{2+} levels inside the spheroids and in the segments between the spheroids (Fig. 4*A–F*). Importantly, the ratiometric property of the Ca^{2+} dye fura-2 controls for the artifacts arising from volume change in the axon. For example, fura-2 reported a similar base level and a rise in Ca^{2+} in the neuronal soma, with its large volume, and in 20–30 μm axonal segments (Fig. 5*A*,*B*).

Analysis of a micrometer-range axoplasmic Ca^{2+} response to H_2O_2 showed a significant difference in Ca^{2+} at the sites of swelling and spheroid formation and the neighboring segments beginning at 15 min. A significantly higher Ca^{2+} level was detected at sites of swellings (Fig. 4*C*,*G*,*H*; 1.90 ± 0.18 vs 1.56 ± 0.13; Student's *t* test, $^{**}p < 0.001$) before formation of spheroids. Subsequent formation of spheroids at 20 min continued to coincide with significantly higher Ca^{2+} within the spheroids than the neighboring segments (Fig. 4*D*,*E*,*G*,*H*; 4.06 ± 0.42 vs 2.63 ± 0.30; Student's *t* test, $^{**}p < 0.001$). Removal of H_2O_2 after 10 min of exposure, when first swellings begin to form (Fig. 4C), prevented spheroid formation but not swellings, which still developed (Fig. 5*C*). Earlier removal of H_2O_2 attenuated further axoplasmic Ca^{2+} rise observed during 30 min exposure to H_2O_2, although axoplasmic Ca^{2+} did not return to baseline within 20 min (Fig. 5*D*). These results suggest the existence of a local Ca^{2+}-regulating mechanism responsible for a significantly higher Ca^{2+} accumulation at the sites of spheroids.

Role of Ca^{2+} sources in spheroid formation

We next compared extracellular and intracellular Ca^{2+} contributions to axoplasmic Ca^{2+} elevation in response to H_2O_2. Varying axonal segments of adult neurons ranging from 2 to 30 μm were analyzed. Elimination of the extracellular Ca^{2+} led to a substantial reduction from 3.6-fold (Fig. 1*C*) to 2-fold by 30 min in fura-2 fluorescence rise and prevented axonal swellings and spheroid formation (Fig. 6*A*,*B*,*I*). Since the absence of extracellular Ca^{2+} did not completely abolish axoplasmic Ca^{2+} increases, the contribution of Ca^{2+} released from mitochondria to the H_2O_2-mediated cytosolic Ca^{2+} increase was next evaluated. Mitochondria released Ca^{2+} during exogenous oxidative stress via formation of permeability transition pore (PTP) (Barsukova et al., 2011b). Consequently, the absence of extracellular Ca^{2+} combined with application of cyclosporin A (CsA, 10 μM, 30 min pretreatment), which binds cyclophilin D (CyPD) and thereby inhibits PTP activation in mitochondria, completely abolished increases in axoplasmic Ca^{2+} (Fig. 6*C*,*D*,*I*) (Forte et al., 2007). CsA

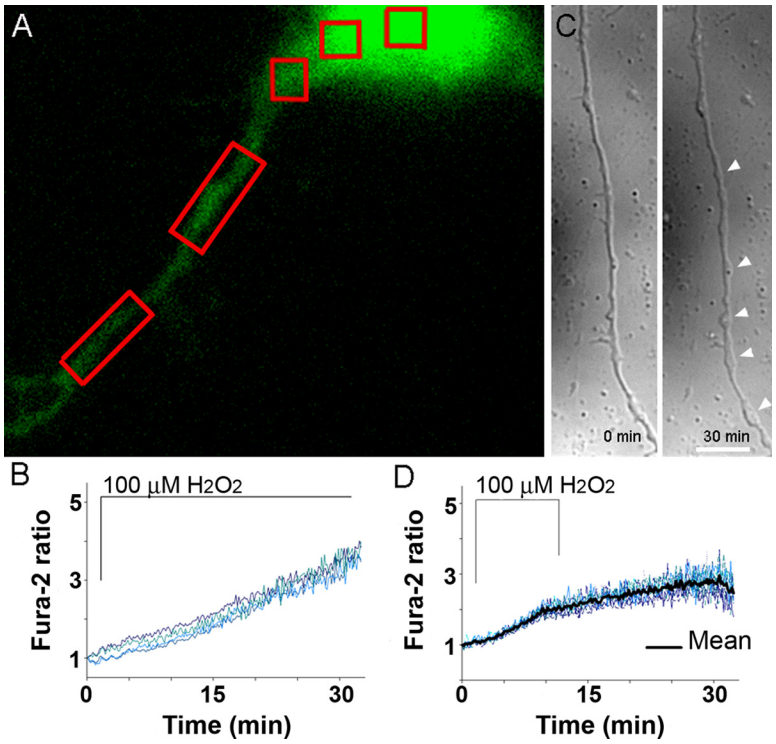

Figure 5. Fura-2 Ca^{2+} reporting is not affected by the sample thickness. ***A***, Fura-2 (green) in a soma and an axon of an adult cortical neuron. In red boxes are areas of interest where Ca^{2+} was analyzed in response to H_2O_2. ***B***, Identical Ca^{2+} increase reported by Fura-2 in a soma and an axon, regions that vary greatly in thickness. ***C***, Removal of H_2O_2 after 10 min, instead of 30 min, results in only swellings and no spheroids by 30 min (right) in an axon of an adult neuron. ***D***, Removal of H_2O_2 attenuates axoplasmic Ca^{2+} increase but does not lower it to baseline, as measured in 20–30 μm segments ($n = 9$ cells; compare response with Fig. 1*C*).

pretreatment alone in the presence of extracellular Ca^{2+} led to a significant axoplasmic Ca^{2+} reduction (Fig. 6*E*,*F*,*I*), and prevented axonal spheroid formation but did not prevent formation of axonal swellings (Fig. 6*E*). Another approach, which also leads to a sustained extracellular Ca^{2+} influx, was tested next. Neurons were subjected to a sustained depolarization with KCl, which led to spheroids formation within 4 min (Fig. 6*H*), strikingly faster when compared with 20 min in response to H_2O_2 (Fig. 1*C*). Fura-2 fluorescence rise reached threefold under KCl at 30 min (Fig. 6*G*). Together, these results demonstrate a primary role of extracellular Ca^{2+} and a secondary role of mitochondrial PTP activation in spheroid formation and axonal severing in response to ROS.

Role of axolemmal Ca^{2+}-regulating systems in spheroid formation

The axolemmal Ca^{2+} regulators, such as the reverse NCX of the plasma membrane and the VGCCs, have been implicated in anoxia, ischemia and MS pathology (Kornek et al., 2001; Pilitsis et al., 2001; Craner et al., 2004a,b; Brand-Schieber and Werner, 2004; Stys 2004, 2005; Annunziato et al., 2007; Tsutsui and Stys, 2012). NCX, operating in reverse mode, could pump Ca^{2+} into the cytoplasm while extruding Na^+, opposite to its normal function of Ca^{2+} extrusion (Tsutsui and Stys, 2012). Consequently, we assessed whether ROS might stimulate reversal of NCX1 and thereby contribute to the axoplasmic Ca^{2+} elevation and spheroid formation. To examine this issue, axonal segments of adult neurons ranging from 2 to 30 μm were analyzed in the presence of the NCX1 inhibitor, KB-R7943, applied within 30 s of H_2O_2 exposure. The results showed that inhibition of NCX1 activity with a single application of KB-R7943 completely prevented swelling and spheroid formation and significantly attenuated axoplasmic Ca^{2+} elevation from 3.6-fold (Fig. 1*C*) to 1.8-fold at 30 min (Fig. 7*A*,*B*,*K*). Moreover, consequent application of KB-R7943 within 14 min of the first application completely abolished axoplasmic Ca^{2+} elevation under H_2O_2 (Fig. 7*C*,*D*,*K*). Remarkably, KB-R7943 completely prevented accelerated swelling and spheroid formation under sustained depolarization with KCl and lowered axoplasmic Ca^{2+} to the baseline by 15 min (compare Figs. 6*G*, *H* and 7*E*, *F*; at 15 min, 2.63 ± 0.72 vs 1.12 ± 0.17; at 30 min; 3.23 ± 0.82 vs 1.00 ± 0.09; Student's *t* test, $^{**}p < 0.0001$). Pretreatment with N-type or L-type VGCC blockers, ω-conotoxin GVIA and amlodipine, respectively, attenuated axoplasmic Ca^{2+} increases, but less than did KB-R7953. Importantly, these blockers also prevented formation of swellings and spheroids (Fig. 7*G*–*K*). These results demonstrate the contributions of the reverse NCX1 and Ca^{2+} channels to axoplasmic Ca^{2+} rise and their key role in spheroid formation in response to ROS.

Aggregation of axolemmal Ca^{2+}-regulating systems in spheroids

Distinct axoplasmic Ca^{2+} elevation within swellings/spheroids during exogenous oxidative stress, demonstrated in Figure 4, could be most easily explained by focal increased influx of extracellular Ca^{2+} at the sites of spheroid formation. This scenario would predict that NCX1 (operating in reverse mode) and N-type VGCC α1B subunit, previously shown to accumulate in axonal lesions in EAE (Kornek et al., 2001; Craner et al., 2004a), accumulate at sites of spheroid formation in response to ROS. Accordingly, we performed immunocytochemistry for these Ca^{2+}-specific regulators implicated in MS in untreated neurons and in neurons exposed to H_2O_2. NCX1 and N-type VGCC α1B subunit were evenly distributed along untreated axons (Fig. 8*A*, *C*). However, after 30 min of H_2O_2 exposure, NCX1 and N-type VGCC α1B subunit were densely aggregated at the sites of axonal spheroids and sparsely distributed in axonal segments between the spheroids (Fig. 8*B*, *D*). Analysis of the fluorescence intensity showed a significant difference in intensity of NCX1 or N-type VGCC α1B immunolabeling between spheroids and axonal areas outside spheroids (Fig. 8*E*). In the absence of the permeabilization step, similar aggregation was observed (Fig. 8*F*, *G*). NCX1 or N-type VGCC α1B accumulation on the axolemma began by 15 min, before spheroid formation (Fig. 8*H*, *I*). Pretreatment of cultures with KB-R7943 or ω-conotoxin attenuated NCX1 or N-type VGCC α1B aggregation and spheroid formation (Fig. 8*J*, *K*). These data demonstrate ROS-driven aggregation of reverse NCX1 and N-type VGCC α1B subunit and suggest that the focal increase in Ca^{2+} at sites of future spheroid formation may result from the aggregation of NCX1 and Ca^{2+} channels at these sites.

Axoplasmic Na^+ in spheroids

If NCX1 operates in reverse mode at sites of axonal swelling, Na^+ would be extruded from the axoplasm by focal aggregation of NCX1 and reflected in uneven dynamic distribution of Na^+

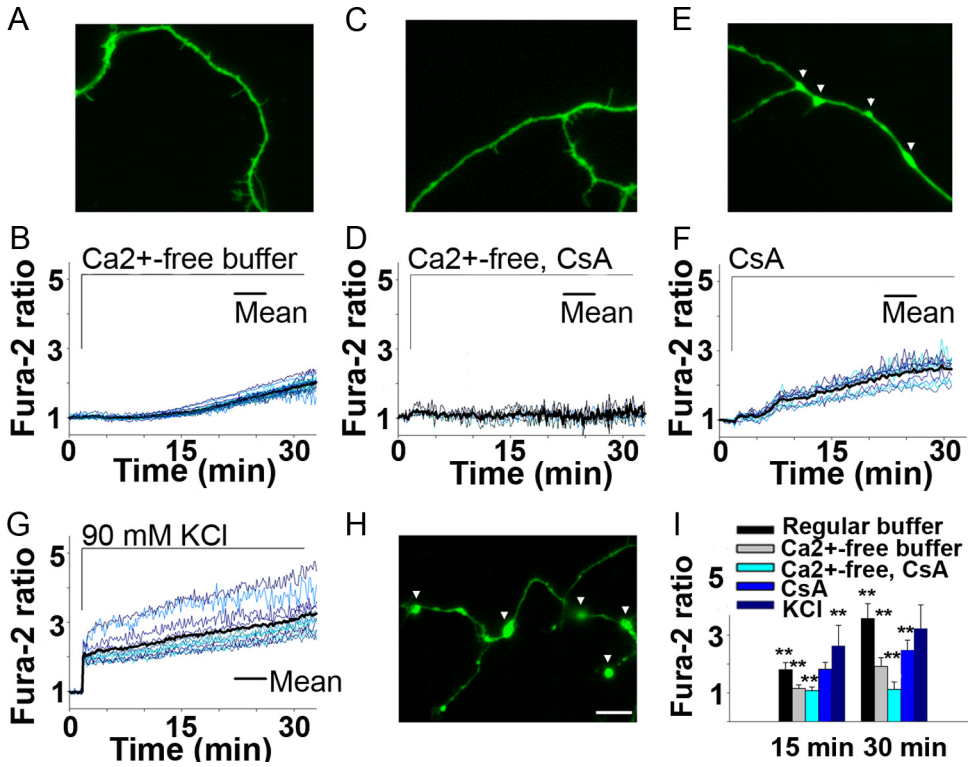

Figure 6. Extracellular and intracellular Ca^{2+} contribution during spheroid formation triggered by ROS in adult neurons. ***A***, ***B***, Absence of extracellular Ca^{2+} prevents swellings/spheroids as it attenuates axoplasmic Ca^{2+} increase during 30 min exposure to 100 μM H_2O_2 and fura-2 (green) ($n = 16$ cells; 150×, oil). Scale bar, 10 μm. ***C***, ***D***, CsA combined with the absence of extracellular Ca^{2+} completely abolishes Ca^{2+} increase and swellings/spheroids ($n = 8$ cells). ***E***, ***F***, CsA in the presence of extracellular Ca^{2+} leads to only swellings and lowers Ca^{2+} increase ($n = 12$ cells). ***G***, ***H***, Sustained depolarization with KCl results in spheroids within 4 min ($n = 11$ cells). ***I***, Ca^{2+} response to above treatments is compared with Ca^{2+} response to H_2O_2 in regular buffer measured in 20–30 μm segments (as shown in Fig. 1*C*) (one-way ANOVA, $^{**}p < 0.001$).

along the axon. To assess this and confirm our earlier results, we also assessed axoplasmic Na^+ in spheroids and neighboring segments with the Na^+-specific ratiometric dye SBFI. Axoplasmic Na^+ increase was significantly lower within spheroids than in the segments outside the spheroids starting at 15 min in response to H_2O_2, as reported by SBFI fluorescence (Fig. 8*L*,*M*; at 15 min, 1.10 ± 0.14 vs 1.38 ± 0.19; at 30 min, 1.40 ± 0.15 vs 1.66 ± 0.21; Student's *t* test, $^{**}p < 0.001$). The difference in Na^+ between spheroids and segments outside is an inverted image of the differences in the case of Ca^{2+} (compare Figs. 4*G*, *H* and 8*L*, *M*). These results are consistent with the demonstrated aggregation of the reverse NCX1 at the sites of spheroids.

Discussion

While ROS-induced axonal spheroid formation and its association with increased axoplasmic Ca^{2+} have been described previously, the molecular details of the connection between Ca^{2+}, spheroid formation, and axonal rupture are uncertain. In the present study, we demonstrate for the first time focal increases of axoplasmic Ca^{2+} that precede spheroid formation in axons exposed to ROS. In addition, we demonstrate the aggregation of the reverse NCX1, N-type VGCC, and actin at sites of focal Ca^{2+} increase and spheroids and the ability to block spheroid formation with inhibitors of NCX1, VGCC, and an actin-stabilizing agent. These findings suggest a series of concerted responses to ROS that lead to focal accumulations of the reverse NCX1 and N-type VGCC and focal increases in axoplasmic Ca^{2+} that result in spheroid formation and axonal disruption.

What key players determined the sites of spheroid formation? Our results show that focal increases in Ca^{2+} preceded spheroid formation. At 15 min of exposure to ROS, Ca^{2+} levels at the sites of future spheroids were significantly higher than in other axonal segments. By 30 min, fura-2 fluorescence rise in spheroids was over 1.5 times higher than in the rest of the axon. This difference in Ca^{2+} levels points to a key role of focal Ca^{2+} increase in spheroid formation. Focal high Ca^{2+} is consistent with transient high Ca^{2+} domains in healthy neurons (Chen et al., 2011). However, during ROS exposure these domains become persistent and mark sites of damage.

Our results demonstrate that extracellular Ca^{2+} is a primary source of ROS-mediated axoplasmic Ca^{2+} increase. Removal of extracellular Ca^{2+} was significantly more efficient in lowering axoplasmic Ca^{2+} and preventing spheroids than inhibition of mitochondrial Ca^{2+} stores release. The inhibition of the reverse NCX1 completely prevented Ca^{2+} increase and spheroid formation in the presence of ROS, suggesting that reverse NCX1 is responsible for the bulk of Ca^{2+} influx. A rise of axoplasmic Na^+ preceded Ca^{2+} increase in response to ROS (Figs. 4*G*,*H*, 8*L*,*M*), suggesting the initial role of Na^+ channels in rising Na^+ and consequent activation of the reverse NCX1. The inhibition of N-type or L-type VGCCs also completely prevented spheroid formation in the presence of ROS and is consistent with neuroprotection achieved with the inhibition of N-type or L-type VGCCs in EAE and blocking N-type VGCC in autoimmune optic neuritis (Kornek et al., 2001; Brand-Schieber and Werner, 2004; Gadjanski et al., 2009). Interestingly, while preventing spheroid formation, blocking N-type or L-type VGCCs did not completely abolish Ca^{2+} rise. What conclusions can be drawn from these findings? First, the reverse NCX1-driven Ca^{2+} contribution is

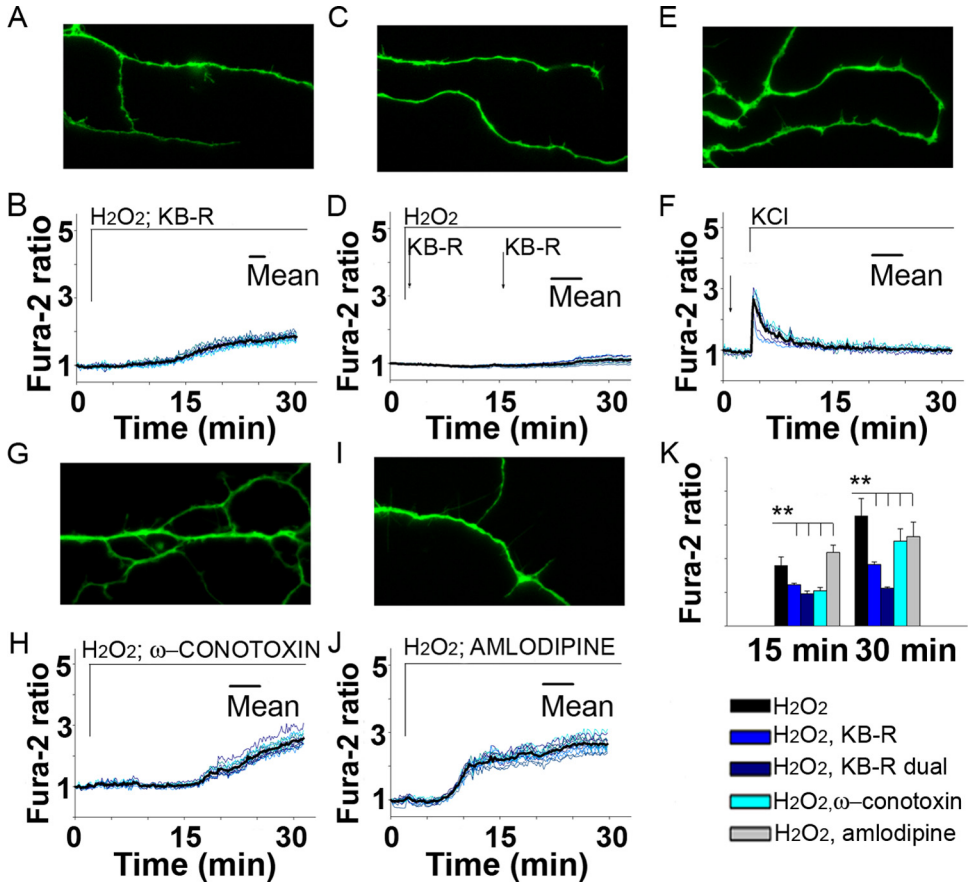

Figure 7. Role of axolemmal Ca^{2+}-regulating systems in spheroid formation triggered by ROS in adult neurons. ***A***, ***B***, KB-R7943, a reverse NCX1 inhibitor, prevents swellings/spheroids as it attenuates axoplasmic Ca^{2+} increase during 30 min exposure to 100 μM H_2O_2 and fura-2 (green) ($n = 12$ cells; 150×, oil). Scale bar, 10 μm. ***C***, ***D***, Dual sequential application of KB-R7943 completely abolishes Ca^{2+} increase and swellings/spheroids during 30 min exposure to H_2O_2 ($n = 10$ cells). ***E***, ***F***, KB-R7943 prevents spheroids and lowers Ca^{2+} during sustained depolarization with KCl ($n = 16$ cells). ***G–J***, ω-Conotoxin (***G***, ***H***), an N-type VGCC inhibitor, and amlodipine (***I***, ***J***), an L-type VGCC inhibitor, prevent swellings/spheroids as they attenuate Ca^{2+} increase ($n = 13$ cells and $n = 14$ cells, respectively). ***K***, Ca^{2+} response to above treatments is compared with Ca^{2+} response to H_2O_2 alone measured in 20–30 μm segments (as shown in Fig. 1*C*) (one-way ANOVA, $^{**}p < 0.001$).

greater than the Ca^{2+} channel-driven Ca^{2+} contribution to ROS-mediated axoplasmic Ca^{2+} rise. Second, both axolemmal reverse NCX1 and Ca^{2+} channels play a key role in spheroid formation. Finally, the formation of spheroids seems to require a certain threshold of Ca^{2+} that needs to be reached, and inhibition of Ca^{2+} channels alone allows a Ca^{2+} rise that does not reach that threshold.

Focal aggregation of reverse NCX1 and N-type VGCC seems to be critical to spheroid formation. Our results show a high density of reverse NCX1 and N-type VGCC within spheroids after exposure to ROS. These findings are consistent with N-type VGCC α1B subunit aggregation in dystrophic axons in EAE and MS (Kornek et al., 2001) and colocalization of NCX and an axonal injury marker, β-amyloid precursor protein, in demyelinated axons in EAE (Craner et al., 2004a). Our data suggest that extracellular ROS lead to active axolemmal changes involving redistribution of NCX1 and VGCC; any swelling solely driven by changes in osmolarity would lead to a spreading of the axolemmal elements, organelles, and cytoskeleton, not focal aggregation. These findings suggest that the aggregation of the reverse NCX1 and N-type VGCC govern the excessive channeling of extracellular Ca^{2+} into the sites of spheroids. Furthermore, opposite dynamics of Ca^{2+} and Na^{+} increases inside and outside the spheroids confirms the role of focal aggregation of the reverse NCX1.

Other intra-axonal changes associated with spheroids were detected. Accumulation of swollen mitochondria in spheroids in response to ROS shown here and previously *in vivo* (Nikić et al., 2011) is likely to occur in response to high focal Ca^{2+} in spheroids, leading to opening of mitochondrial PTP (Barsukova et al., 2011b). It is plausible that ROS-driven activation of the PTP, loss of ATP, and release of pro-apoptotic agents are primary events responsible for spheroid formation. However, pretreatment of neurons with CsA, which inhibits PTP activation, did not prevent axonal swellings during ROS exposure. These results point to a secondary role of ROS-driven mitochondrial dysfunction in spheroid formation. A high density of fluorescent labeling for F-actin was found in spheroids. Since Ca^{2+} regulates actin dynamics (Brünig et al., 2004; Oertner and Matus, 2005; Akopian et al., 2006), F-actin aggregation within spheroids is likely to stem from the effect of Ca^{2+} rise on normal F-actin concentration at branching points (Andersen et al., 2011). Indeed, the majority of spheroids formed at branching points along the axon (Fig. 2*A*,*B*). Retraction of small branches preceded formation of spheroids at branching sites. Attenuation of spheroid formation with the actin-stabilizing agent cytochalasin D, shown here, and the reversible nature of spheroid formation previously shown *in vivo* (Nikić et al., 2011) support the idea that active cytoskeletal restructuring occurs in response to ROS. Furthermore, it is consistent with the previous findings that depolymerization of actin

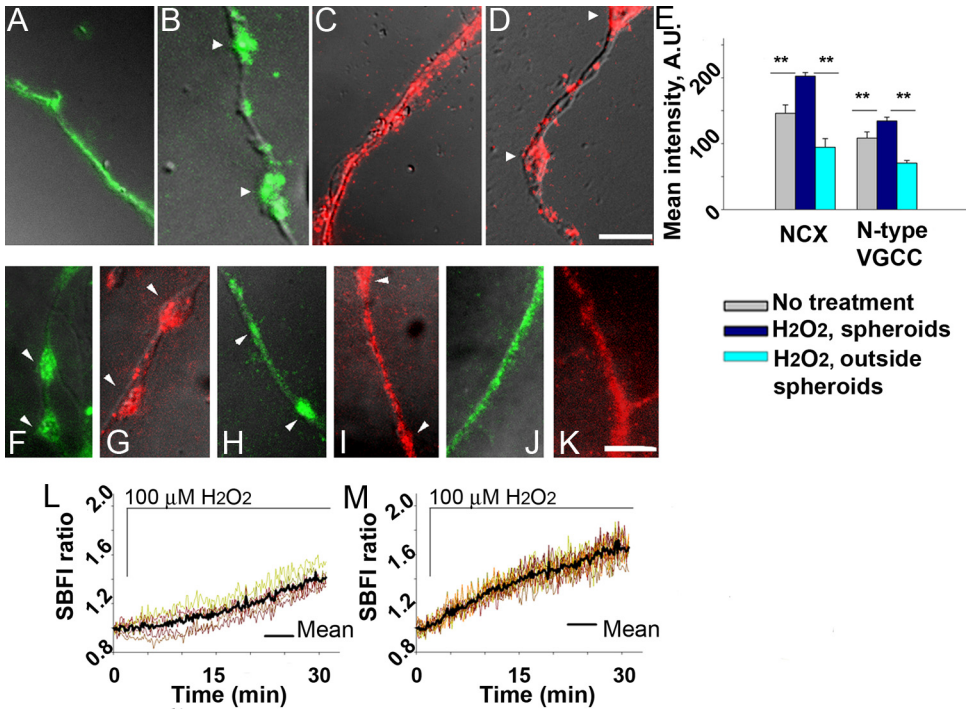

Figure 8. Aggregation of axolemmal Ca^{2+}-regulating systems during spheroid formation triggered by ROS in adult neurons. ***A***, NCX1 distribution in an untreated axon (green) (150×, oil). Scale bar, 5 μm. ***B***, NCX1 aggregation in spheroids at 30 min of exposure to 100 μM H_2O_2 ($n = 15$ cells). ***C***, N-type VGCC α1B subunit (red) distribution in an untreated axon. ***D***, N-type VGCC α1B subunit aggregation in spheroids at 30 min of exposure to 100 μM H_2O_2 ($n = 14$ cells). ***E***, Quantification of fluorescence intensities of NCX1 and N-type VGCC α1B subunit immunolabeling (one-way ANOVA, $^{**}p < 0.001$). ***F***, ***G***, NCX1 (green) and N-type VGCC α1B subunit (red) aggregation in axolemma of spheroids at 30 min of exposure to 100 μM H_2O_2, in the absence of permeabilization ($n = 9$ cells and $n = 10$ cells, respectively). ***H***, ***I***, NCX1 and N-type VGCC α1B subunit aggregation before spheroid formation, at 15 min of exposure to H_2O_2 ($n = 12$ cells and $n = 11$ cells, respectively). ***J***, ***K***, Attenuation of NCX1 and N-type VGCC α1B subunit aggregation in the presence of KB-R7943 or ω-conotoxin ($n = 14$ cells and $n = 12$ cells, respectively). ***L***, ***M***, Axoplasmic Na^+ response during spheroid formation triggered by ROS in adult neurons ($n = 12$ cells). ***L***, Na^+ levels at the sites of spheroids. ***M***, Na^+ levels in axonal segments between the spheroids.

with cytochalasin D stabilizes intracellular free Ca^{2+} and protects hippocampal neurons (Furukawa et al., 1995). Actin thus may play a dual role in the formation of spheroids: a structural and a Ca^{2+}-regulating role. While a high density of the punctuate fluorescent labeling for tubulin occurred in spheroids, suggesting the presence of disrupted microtubules, Taxol, which stabilizes microtubules, did not prevent spheroid formation, suggesting a secondary role of microtubule destabilization.

Together, these results suggest the following scenario of axonal spheroid formation in response to ROS. Elevated exogenous H_2O_2 associated with pathologic inflammation (Nikić et al., 2011) leads to axoplasmic Na^+ increase. Rising Na^+ activates the reverse mode of NCX, leading to a fast uniform Ca^{2+} increase along the axon. Rising Ca^{2+} leads to further aggregation of F-actin normally found concentrated at axonal branching points and axon terminals. Fast actin response and its aggregation is likely to drive axolemmal changes, such as aggregation of reverse NCX and VGCCs. Increased focal density of reverse NCX and VGCC results in focal Ca^{2+} increases at the sites of axonal swelling. Disrupted axonal transport contributes to swellings progressing into spheroids. Rapidly rising focal Ca^{2+} in spheroids triggers local mitochondrial Ca^{2+} overload, PTP activation, and release of pro-apoptotic agents. Removal of ROS or application of antioxidants reverses the direction of NCX, allowing for the extrusion of axoplasmic Ca^{2+} excess, deaggregation of actin, and restoration of axonal transport.

This study does not address cellular sources of ROS that occur *in vivo*, such as activated microglia, and whether ROS-producing inflammatory cells would induce focal Ca^{2+} rise at sites of spheroid formations. Our *in vitro* system contains unmyelinated axons, and whether myelinated axons would develop focal Ca^{2+} increases at sites of spheroid formations in response to ROS is also uncertain. However, our study may be of relevance to MS, in which loosely myelinated or demyelinated segments present an unprotected axonal surface for interaction with elevated levels of ROS produced by microglia in MS lesions (Lassmann, 2010; Abourbeh et al., 2012). Importantly, demyelination in MS leads to $Na_v1.6$ and $Na_v1.2$ channel redistribution (Craner et al., 2004b) and their increase in demyelinated segments. That would facilitate focal Na^+ rise, reversal of NCX and Ca^{2+} rise, which makes our proposed model of Ca^{2+}-dependent spheroid formation even more relevant to MS. Upregulation of Na+ influx shown here is also characteristic of trauma (Iwata A et al., 2004) and anoxia/ischemia, suggesting that the proposed model is a common pathway for axonal degeneration. While the relative specificity of KB-R7943 could be a limitation at 10 μM via nonspecific block of L-type Ca^{2+} channels (Ouardouz et al., 2005), we used an order of magnitude lower concentration of 1 μM KB-R7943. Importantly, when L-type Ca^{2+} channels were blocked with amlodipine, we saw only a modest effect on axoplasmic Ca^{2+} regulation (Fig. 7, *J* vs *B*, *D*). These results implicate the influx of Ca^{2+} via reverse NCX1 as a key event in the onset of spheroid formation. CsA binds not only to CyPD in mitochondria but other cyclophilins as well. However, CsA pretreatment did not affect the cytosolic Ca^{2+} level in adult neurons in which CyPD was genetically eliminated but other cyclophilins remained intact (our unpublished observations). Therefore, we believe CsA was sufficiently specific for the assessment of the contribution of mitochondria to increases in axoplasmic Ca^{2+} in response to ROS.

In summary, our findings suggest that ROS-mediated spheroid formation is driven by three main events: fast actin response and its aggregation, focal aggregation of NCX and VGCC, and focal Ca^{2+} rise. These results create a basis for developing new neuroprotective strategies that would prevent spheroid formation by targeting Ca^{2+}–actin interactions and Ca^{2+} regulating systems—actin interactions in axons undergoing oxidative stress.

References

Abourbeh G, Thézé B, Maroy R, Dubois A, Brulon V, Fontyn Y, Dollé F, Tavitian B, Boisgard R (2012) Imaging microglial/macrophage activation in spinal cords of experimental autoimmune encephalomyelitis rats by positron emission tomography using the mitochondrial 18 kDa translocator protein radioligand [18F]DPA-714. J Neurosci 32:5728–5736.

Akopian A, Szikra T, Cristofanilli M, Krizaj D (2006) Glutamate-induced Ca2+ influx in third-order neurons of salamander retina is regulated by the actin cytoskeleton. Neuroscience 138:17–24.

Andersen EF, Asuri NS, Halloran MC (2011) In vivo imaging of cell behaviors and F-actin reveals LIM-HD transcription factor regulation of peripheral versus central sensory axon development. Neural Dev 6:27.

Annunziato L, Pignataro G, Boscia F, Sirabella R, Formisano L, Saggese M, Cuomo O, Gala R, Secondo A, Viggiano D, Molinaro P, Valsecchi V, Tortiglione A, Adornetto A, Scorziello A, Cataldi M, Di Renzo GF (2007) ncx1, ncx2, and ncx3 gene product expression and function in neuronal anoxia and brain ischemia. Ann N Y Acad Sci 1099:413–426.

Barsukova A, Komarov A, Hajnóczky G, Bernardi P, Bourdette D, Forte M (2011a) Activation of the mitochondrial permeability transition pore modulates Ca2+ responses to physiological stimuli in adult neurons. Eur J Neurosci 33:831–842.

Barsukova AG, Bourdette D, Forte M (2011b) Mitochondrial calcium and its regulation in neurodegeneration induced by oxidative stress. Eur J Neurosci 34:437–447.

Beirowski B, NógrádiA, Babetto E, Garcia-Alias G, Coleman MP (2010) Mechanisms of axonal spheroid formation in central nervous system Wallerian degeneration. J Neuropathol Exp Neurol 69:455–472.

Brand-Schieber E, Werner P (2004) Calcium channel blockers ameliorate disease in a mouse model of multiple sclerosis. Exp Neurol 189:5–9.

Brünig I, Kaech S, Brinkhaus H, Oertner TG, Matus A (2004) Influx of extracellular calcium regulates actin-dependent morphological plasticity in dendritic spines. Neuropharmacology 47:669–676.

Chen X, Leischner U, Rochefort NL, Nelken I, Konnerth A (2011) Functional mapping of single spines in cortical neurons in vivo. Nature 475:501–505.

Coleman M (2005) Axon degeneration mechanisms: commonality amid diversity. Nat Rev Neurosci 6:889–898.

Craner MJ, Hains BC, Lo AC, Black JA, Waxman SG (2004a) Colocalization of sodium channel Nav1.6 and the sodium-calcium exchanger at sites of axonal injury in the spinal cord in EAE. Brain 127:294–303.

Craner MJ, Newcombe J, Black JA, Hartle C, Cuzner ML, Waxman SG (2004b) Molecular changes in neurons in multiple sclerosis: altered axonal expression of Nav1.2 and Nav1.6 sodium channels and Na+/Ca2+ exchanger. Proc Natl Acad Sci U S A 101:8168–8173.

Forte M, Gold BG, Marracci G, Chaudhary P, Basso E, Johnsen D, Yu X, Fowlkes J, Rahder M, Stem K, Bernardi P, Bourdette D (2007) Cyclophilin D inactivation protects axons in experimental autoimmune encephalomyelitis, an animal model of multiple sclerosis. Proc Natl Acad Sci U S A 104:7558–7563.

Furukawa K, Smith-Swintosky VL, Mattson MP (1995) Evidence that actin depolymerization protects hippocampal neurons against excitotoxicity by stabilizing [Ca2+]i. Exp Neurol 133:153–163.

Gadjanski I, Boretius S, Williams SK, Lingor P, Knöferle J, Sättler MB, Fairless R, Hochmeister S, Sühs KW, Michaelis T, Frahm J, Storch MK, Bähr M, Diem R (2009) Role of n-type voltage-dependent calcium channels in autoimmune optic neuritis. Ann Neurol 66:81–93.

Hyslop PA, Zhang Z, Pearson DV, Phebus LA (1995) Measurement of striatal H2O2 by microdialysis following global forebrain ischemia and reperfusion in the rat: correlation with the cytotoxic potential of H2O2 in vitro. Brain Res 671:181–186.

Iwata A, Stys PK, Wolf JA, Chen XH, Taylor AG, Meaney DF, Smith DH (2004) Traumatic axonal injury induces proteolytic cleavage of the voltage-gated sodium channels modulated by tetrodotoxin and protease inhibitors. J Neurosci 19:4605–4613.

Kornek B, Storch MK, Bauer J, Djamshidian A, Weissert R, Wallstroem E, Stefferl A, Zimprich F, Olsson T, Linington C, Schmidbauer M, Lassmann H (2001) Distribution of a calcium channel subunit in dystrophic axons in multiple sclerosis and experimental autoimmune encephalomyelitis. Brain 124:1114–1124.

Lassmann H (2010) Axonal and neuronal pathology in multiple sclerosis: what have we learnt from animal models. Exp Neurol 225:2–8.

Nathan BP, Barsukova AG, Shen F, McAsey M, Struble RG (2004) Estrogen facilitates neurite extension via apolipoprotein E in cultured adult mouse cortical neurons. Endocrinology 145:3065–3073.

Nikić I, Merkler D, Sorbara C, Brinkoetter M, Kreutzfeldt M, Bareyre FM, Bruck W, Bishop D, Misgeld T, Kerschensteiner M (2011) A reversible form of axon damage in experimental autoimmune encephalomyelitis and multiple sclerosis. Nat Med 17:495–499.

Oertner TG, Matus A (2005) Calcium regulation of actin dynamics in dendritic spines. Cell Calcium 37:477–482.

Ouardouz M, Zamponi GW, Barr W, Kiedrowski L, Stys PK (2005) Protection of ischemic rat spinal cord white matter: dual action of KB-R7943 on Na+/Ca2+ exchange and L-type Ca2+ channels. Neuropharmacology 48:566–575.

Pilitsis JG, Diaz FG, O'Regan MH, Phillis JW (2001) Inhibition of Na(+)/Ca(2+) exchange by KB-R7943, a novel selective antagonist, attenuates phosphoethanolamine and free fatty acid efflux in rat cerebral cortex during ischemia-reperfusion injury. Brain Res 916:192–198.

Sayre LM, Perry G, Smith MA (2008) Oxidative stress and neurotoxicity. Chem Res Toxicol 21:172–188.

Stys PK (2004) White matter injury mechanisms. Curr Mol Med 4:113–130.

Stys PK (2005) General mechanisms of axonal damage and its prevention. J Neurol Sci 233:3–13.

Tsutsui S, Stys PK (2012) Metabolic injury to axons and myelin. Exp Neurol. Advance online publication. Retrieved May 1, 2012. doi:10.1016/j.expneurol.2012.04.016.

Wang JT, Medress ZA, Barres BA (2012) Axon degeneration: Molecular mechanisms of a self-destruction pathway. J Cell Biol 196:7–18.